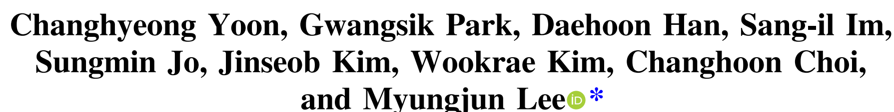

# Toward realization of high-throughput hyperspectral imaging technique for semiconductor device metrology

**Changhyeong Yoon, Gwangsik Park, Daehoon Han, Sang-il Im, Sungmin Jo, Jinseob Kim, Wookrae Kim, Changhoon Choi, and Myungjun Lee***

Samsung Electronics Co., Ltd., Mechatronics Research, Equipment R&D Team 4, Inspection Solution Group, Hwasung-si, Republic of Korea

## Abstract

**Background:** High-throughput three-dimensional metrology techniques for monitoring in-wafer uniformity (IWU) and in-cell uniformity (ICU) are critical for enhancing the yield of modern semiconductor manufacturing processes. However, owing to physical limitations, current metrology methods are not capable of enabling such measurements. For example, the optical critical dimension technique is not suitable for ICU measurement, because of its large spot size. In addition, it is excessively slow for IWU measurement.

**Aim:** To overcome the aforementioned limitation, we demonstrate a line-scan hyperspectral imaging (LHSI) system, which combines spectroscopy and imaging techniques to provide sufficient information for spectral and spatial resolution, as well as high throughput.

**Approach:** The proposed LHSI system has a 5-$\mu$m spatial resolution together with 0.25-nm spectral resolution in the broad-wavelength region covering 350 to 1100 nm.

**Results:** The system enables the simultaneous collection of massive amounts of spectral and spatial information with an extremely large field of view of $13 \times 0.6\ \text{mm}^2$. Additionally, throughput improvement by a factor of $10^3$ to $10^4$ can be achieved when compared with standard ellipsometry and reflectometry tools.

**Conclusions:** Owing to its high throughput and high spatial and spectral resolutions, the proposed LHSI system has considerable potential to be adopted for high-throughput ICU and IWU measurements of various semiconductor devices used in high-volume manufacturing.

© *The Authors. Published by SPIE under a Creative Commons Attribution 4.0 International License. Distribution or reproduction of this work in whole or in part requires full attribution of the original publication, including its DOI.* [DOI: 10.1117/1.JMM.21.2.021209]

**Keywords:** critical dimension uniformity; semiconductor; metrology; optical critical dimension; hyperspectral imaging.

Paper 21091SS received Nov. 4, 2021; accepted for publication Mar. 29, 2022; published online Apr. 20, 2022.

## 1 Introduction

In recent years, as the semiconductor manufacturing process continues to become complex and the device sizes continue to shrink, reduced production due to uniformity of critical dimension (CD) becomes a critical concern. A minor CD fluctuation in each process step that may not have affected the performance of the device seriously for the previous generation of semiconductor devices, is now gradually reducing the yield.[1]

In addition, the semiconductor industry has entered a super cycle in which the demand for chips has significantly increased, and therefore high-speed manufacturing throughput has emerged as the most important concern. Therefore, there is an increasing demand for advanced metrology and inspection (MI) techniques that enable fast and accurate monitoring of the in-cell uniformity (ICU) in semiconductor devices.[2–4] It is important to note that increasing the speed of

*Address all correspondence to Myungjun Lee, myung01.lee@samsung.com; mjlee.optic@gmail.com

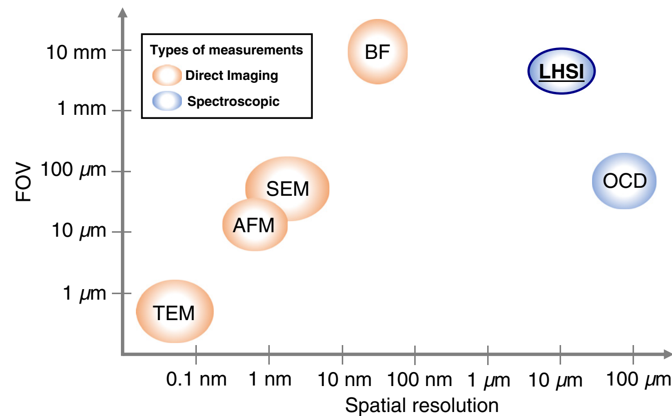


**Fig. 1** Performance comparison for various metrology and inspection techniques as a function of resolution and FOV. LHSI provides relatively larger FOV with higher spatial resolution among spectroscopic techniques, resulting in precise measurement of the ICU and IWU. Note that the FOV for the bright field and HSI tools were calculated by converting the area scanned for 1 s into the area of the square. The FOV for other techniques was defined by the diagonal length of the measured image. Note that TEM stands for transmission electron microscopy.

the feedback cycle of the advanced process control based on various MI results is the key to yield enhancement. However, existing metrology methods, including scanning electron microscopy (SEM),[5,6] atomic force microscopy (AFM),[7,8] and optical scatterometry,[9–12] have throughput limitations because of the physical trade-off between resolution and field of view[13–15] (FOV), as illustrated in Fig. 1. For example, SEM is one of the representative imaging-based MI methods; its nanoscale imaging enables intuitive CD measurement. It is widely used as the referencing tool for modeling in-direct imaging methods such as ellipsometry and reflectometry. However, the data acquisition speed of SEM is too slow to measure the IWU due to its narrow FOV and the associated high electron energy might increase the risks that could damage photosensitive materials during the manufacturing process.[16,17] As compared to SEM and AFM techniques, scatterometry [also called optical critical dimension (OCD) spectroscopy] can provide a relatively larger FOV (i.e., typically tens of $\mu$m to 200 $\mu$m), which enables the fast and reliable monitoring of the critical parameters of chip structures.[1] However, OCD is a spot-based metrology technique, providing an averaged CD value over a large spot size of approximately $25 \times 30\ \mu\mathrm{m}^2$, thus, it is practically difficult to observe CD uniformity in a dynamic random-access memory (DRAM) cell or mat in vertical not-and flash memory (VNAND) chip. For these reasons, a unique three-dimensional (3D) metrology technique that can provide high spatial resolution and high throughput, simultaneously, is necessary for accurate ICU and IWU measurements.

Recently, several researchers have focused on the implementation of the hyperspectral imaging (HSI) technique to increase spatial resolution and throughput, simultaneously.[18–23] The HSI method entails combining spectroscopy and scattering techniques with a microscopic approach.[24,25] Such methods have been employed for biomedical imaging,[26–28] surface inspection,[29,30] film metrology,[31–35] and other types of applications,[36,37] with different illumination geometry, such as normal illumination and oblique illumination. Nonetheless, many of the above-mentioned techniques are still not mature enough to apply for wafer measurement in a semiconductor fabrication plant (FAB). As an example, a normal illumination-based HSI system does not provide high enough sensitivity for the measurement of the tiny semiconductor structures compared to standard OCD measurement.[29–31] Furthermore, the application of using a narrow wavelength range in the HSI reduces the measurement accuracy.[30–33] It is important to note that developing the broadband HSI system is very challenging due to the use of an imaging lens. In addition, when a monochromator is used, it is practically difficult to obtain accurate spectra because of the low spectral resolution of approximately 5- to 10-nm band steps. Such low spectral resolution makes it hard to obtain an accurate spectrum, especially in a high-aspect-ratio structure, such as a channel hole (Ch.H.) array in VNAND.

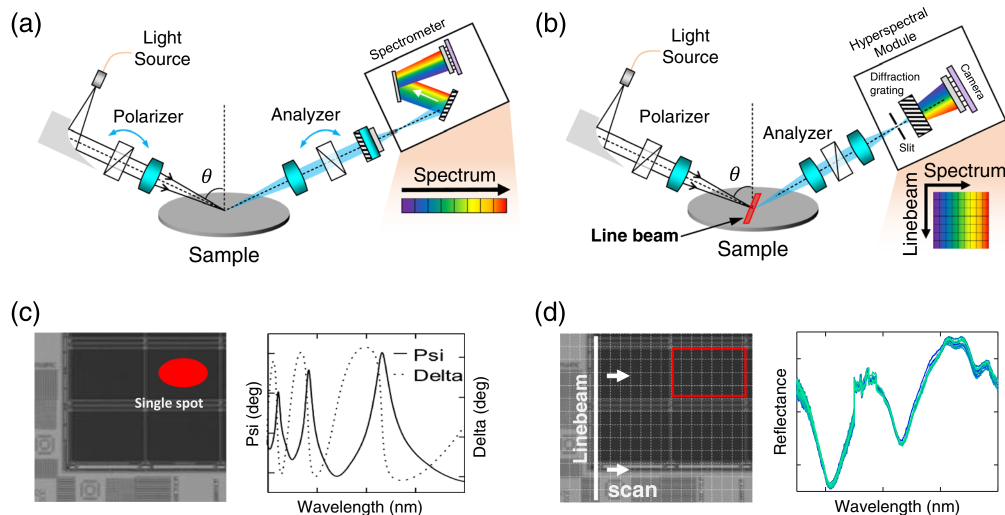


**Fig. 2** Comparison of standard OCD versus LHSI systems. (a) Optical system for conventional OCD measurement. The detected signal is a single spectrum of the illumination point. (b) Schematic of the proposed LHSI system. Here, the wafer is scanned by using a narrow line beam, where the 2D dispersed image $(x, \lambda)$ can be collected by an area scan camera. (c) and (d) shows the measurements results of the single cell in a DRAM device using two different metrology techniques (a) and (b), respectively. The OCD illumination spot size fits in a single cell in DRAM, providing the SE measurement data $(\Psi, \Delta)$ only including structure information of the average value at the single illumination spot shown in (c). However, the grid box size in (d) denotes the spatial resolution or effective spot size in the LHSI system, and therefore one can obtain the spectrum from a much smaller area, as shown in the grid box. It can be seen that the spatial sampling is much higher compared to that of OCD spectroscopy, suitable for ICU measurement. Spectra were collected at more than 10 different points in the single DRAM cell represented by the area marked in a red box, which shows the spectral variation caused by the actual CD changes.

Herein, we propose a line-scan hyperspectral imaging (LHSI) system that provides high throughput together with high spatial and spectral resolution suitable for ICU and IWU measurements. As compared to the standard OCD systems, the LHSI is able to provide much more detailed information about the structure variations in the single memory and static random-access memory cell by obtaining and analyzing the massive amount of spectral data. Figure 2 describes the schematic and performance comparison between OCD spectroscopy and the proposed LHSI system.[38] The main differences in optics configuration are the illumination shape at the wafer and the detection method. In the case of OCD spectroscopy, a wafer is illuminated by a focused circular-shaped beam on the wafer, and spectroscopic detection is performed to obtain the spectrum for a single illumination spot, as shown in Fig. 2(a). Typically, the size of the illumination spot in the visible wavelength range is approximately 25 $\mu$m × 30 $\mu$m owing to oblique illumination conditions and low-numerical aperture (NA) focusing. Because of the relatively larger spot size, the area of illumination in a DRAM cell is too large to measure the local CD variations within a single memory cell, as shown in Fig. 2(c).

Alternatively, in the case of LHSI, we can actually image the area of our interests for various wavelengths, obtaining the spectra from each pixel in the images. Figure 2(b) shows a schematic of the LHSI system, which captures dispersive light $(x, \lambda)$, where the two-dimensional (2D) wafer image $(x, y)$ can be obtained by scanning a wafer with a line beam. This configuration allows us to obtain spectra for a much smaller effective spot size with a millimeter-scale FOV. Moreover, the spectrum can be resolved with a high spectral resolution by using a high-pixel-resolution camera. As described in Fig. 2(d), the spatial resolution of the LHSI is reflected in the grid size of the DRAM image, which serves to increase the acquisition rate of spatial information by more than 30 times that of the OCD spectroscopic technique. As a result, it is possible to observe the spectral variation for each position within a single cell and mat of the semiconductor devices, providing the capability to accurately measure the in-cell, in-chip, and in-wafer uniformity.

## 2 System Configuration

In this section, the LHSI system designed for high throughput wafer metrology is presented. The proposed system can image the reflected light at various wavelengths from the film and patterned structures on a semiconductor wafer to measure the thickness of each thin-film layer, as well as the CD of semiconductor structures. The LHSI system, as shown in Fig. 3, is capable of large-area imaging with high lateral resolution. This allows the system to perform higher throughput measurements than the conventional spectroscopic ellipsometry (SE) system.

In the LHSI system, a laser-driven light source (LDLS) is used to generate broadband light with a range of 170 to 2500 nm, and it is propagated through illumination optics that includes a focusing mirror, a polarizer, and relay optics. The optical component in this proposed LHSI system is optimized to cover the light from 350 to 1100 nm, where the camera quantum efficiency (QE), diffraction grating efficiency, and the practical difficulty of the high-reflection coating for broadband were incorporated into the system design. The broadband light reflected from the focusing mirror passes through the polarizer to define the incident polarization state, as shown in Fig. 3(a). It is important to mention that this illumination optics sub-system has an NA of 0.08, and can generate a line beam that has a rectangular shape with dimensions of 13 mm × 1 mm in Fig. 3(b). Additionally, the line beam is focused on the wafer surface at a set angle of incidence of 65 deg, which is close to Brewster's angle for a silicon wafer. Note that Brewster's angle is the angle of incidence associated with no reflection of the *p*-polarization state at the optical surface.[39] It is commonly applied in SE measurements because the SE signal has the highest sensitivity near this angle. By scanning the wafer in a direction that is perpendicular to the longer axis of the line beam, high-throughput, wide-area imaging can be realized.

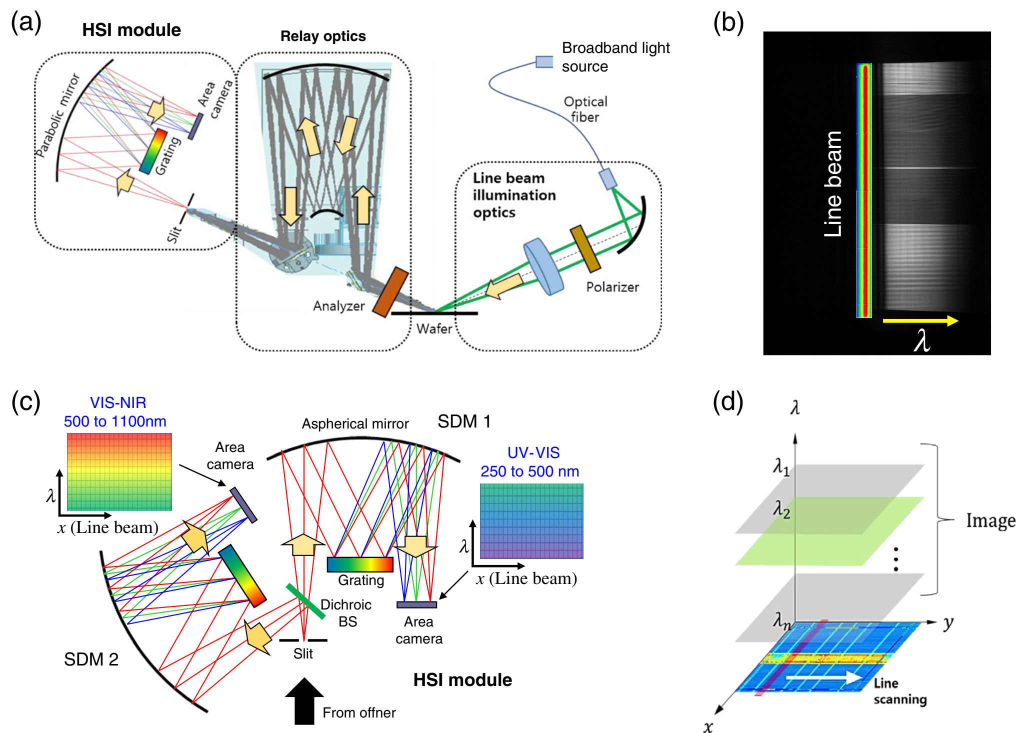


**Fig. 3** LHSI optics methodology. (a) Schematic illustration of LHSI optics methodology. A wafer is scanned by a broadband line beam with dimensions of $13 \times 1\ \mathrm{mm}^2$, and the reflected signal is dispersed and detected by a 2D area camera. (b) The raw image detected by the camera. The broadband line beam is dispersed along the wavelength axis. For clear and accurate spectral imaging, a compensation process should be applied. (c) HSI module, which consists of two SDMs. The reflected signal is cropped by a slit to enhance the imaging performance and increase the spectral resolution. Two SDMs and a detector are used applied to cover the 350 to 1100 nm broadband without spectral error. (d) 3D data cube generated by the LHSI system. Specifically, it is generated by stacking the line beam image for each scan position.

The reflected light from the semiconductor wafer is delivered to an analyzer and the relay optics to project an image of the wafer toward the dispersive modules. Additionally, an Offner relay is employed as the relay optics in the LHSI system. It is a well-known 1:1 reflective imaging system comprising two concentric spherical mirrors that create an image under telecentric conditions.[40] An advantage of using an Offner relay is that constant magnification can be applied regardless of the occurrence of defocusing and it also yields low image distortion. In addition, the use of the Offner relay affords system compactness through the implementation of an optimized optical design. The polarization state of the reflected light is selected by the analyzer before the light reaches the Offner relay system. The light at the wafer conjugate plane of the Offner relay system passes through the spectral dispersive module, as illustrated in Fig. 3(a), forming line beam images for each wavelength at the detector plane. Without proper spatial filtering, the undesired spectral overlap is inevitable because the width of the line beam image is not sufficiently narrow at the camera. As a result, the achievable spectral resolution can be degraded due to the reception of multiple wavelengths of light into each pixel of the camera, simultaneously. To avoid the above-mentioned issue, a narrow-width slit, as shown in Fig 3(a), is employed in the LHSI system to improve the spectral resolution through the process of filtering by only taking the center of the line beam to minimize the range of the overlapping wavelengths. Employing the slit improves the imaging performance for LHSI as well as spectral resolution. Figure 3(b) shows a dispersed line beam image captured by a camera. It is important to note that the uniformity of intensity distribution along the line beam is also important to obtain high-quality spectral images for each position of the line beam throughout the scanning process. By cropping the uniform intensity distribution region of the line beam through the slit, it is possible to minimize the variation in the intensity distribution in the reconstructed spectral image. Moreover, the image contrast and spatial resolution can be improved by blocking out-of-focus light in a manner similar to the working principle of confocal microscopy.[41]

The width of the slit should be determined by taking into consideration the factors that affect system resolution, such as the camera pixel size, magnification, and optical power loss, and here our LHSI system design includes an optimal slit width of 10 $\mu$m. The spatial resolution of the LHSI system was designed to be approximately 5 $\mu$m in both $x$ and $y$ directions at the intermediate wavelength of 700 nm after taking into consideration the imaging conditions of the Offner relay and slit width. This corresponds to an effective spot size that is 30 times smaller than the spot size that can be achieved by conventional OCD tools.

After spatial filtering occurs at the slit, the light is delivered to the HSI modules. Because of the limitations associated with the application of single diffraction grating and a single camera sensor to broadband light, the HSI module should consist of two separate spectral dispersive modules (SDM) that are customized for the relevant wavelength ranges, as shown in Fig. 3(c). According to the basic principle of the diffraction grating, low-order diffraction light and higher-order light may overlap when the broadband light is incident. For example, when a light wavelength in the range of 350 to 700 nm is diffracted by a grating, the peak positions of the second-order diffraction of 350 nm and first-order diffraction of 700 nm may be the same. This generates critical errors in the spectral measurements. Thus, the SDM was designed to be a combination of modules for two wavelength bands. Regarding the HSI module, once the light reaches the slit, it is split into two by a short-pass dichroic beam splitter (cut-on wavelength: 500 nm), which allows each beam to propagate toward each of the SDMs, as illustrated in Fig. 3(c).

One SDM module was designed to cover the shorter wavelength region of the near-ultraviolet (NUV)-visible (VIS) band (i.e., from 350 to 500 nm), whereas the other module was designed to cover the longer wavelength region of the VIS-near-infrared (NIR) band (i.e., from 500 to 1100 nm). To realize high-performance LHSI, the Offner spectrometer was designed for application to the SDM to ensure that an accurate dispersive slit image is displayed at the camera sensor. Instead of employing a common Offner spectrometer which consists of a spherical mirror and curved diffraction grating,[40] an aspherical mirror and a plane diffraction grating were employed to reduce optical aberrations and improve the LHSI system performance. A blazed grating has also been incorporated to increase the diffraction efficiency (NUV-VIS: Newport 100 groove/mm, VIS-NIR: Shimadzu 200 groove/mm). The reflected light from the side of the aspherical mirror is directed through a blazed grating, which then disperses the broadband light

into light components according to wavelength. Finally, the dispersed light is reflected back to the opposite edge of the aspherical mirror and delivered to a camera. To optimize the imaging performance and maximize the throughput, two back-side illumination sCMOS cameras (Kinetix, Teledyne Dalsa) were adopted as the LHSI detector to obtain spectral images with high QE in the UV and IR ranges. Each camera has a physical pixel size of 6.5 $\mu$m and offers a high pixel resolution of $3200 \times 3200$, which allows for fine spectral sampling, as well as a high spatial sampling rate. In particular, the window in front of the camera sensor has been customized to act as continuously variable spectral filters along the wavelength axis in order to prevent high-order diffracted light generated from gratings. Here, two cameras simultaneously record 2D images $(x, \lambda)$ of a line beam dispersed along the wavelength axis, as shown in Figs. 3(b) and 3(c). In each SDM camera, dispersed light is extended up to 1000 pixels along the wavelength axis, consequently affording sub-nm spectral resolution; specifically, 0.25 nm/pixel and 0.8 nm/pixel for the NUV-VIS and VIS-NIR, respectively. A wide-field wafer imaging can be realized by scanning the wafer in the vertical direction of the line beam. Regarding the optical conditions of the LHSI system, the achievable scan speed is 0.6 mm/s with 110.50 fps of the camera, corresponding to the maximized FOV of 13 mm $\times$ 0.6 mm per 1 s, which is 10,000 times larger than that of the single measurement in conventional OCD technique. Synthesis of the scanned images captured by the two SDMs yields a 3D massive data cube $(x, y, \lambda)$ with a wavelength range of 350 to 1100 nm, as described in Fig. 3(d).

## 3 Experimental Results

### 3.1 *System Calibration and Data Processing*

In this section, we present the measurement results of the LHSI system for both non-patterned and patterned wafers. In the first experiment, the thickness of the thin film wafer was measured to verify the performance of the system. It allowed us to validate the performance of the system and process of data compensation to ensure accurate spectrum analysis, which was performed by evaluating the theoretical results with respect to the corresponding experimental data and applying optical parameters to achieve spectral matching between them. The theoretical spectrum was obtained for a thin film by applying the relevant optical parameters, such as the refractive index and absorption coefficient of the thin-film medium, the illumination angle, and the angular distribution of illumination, to calculate the thin-film interference and Fresnel coefficients.[39] Through the process of finely adjusting various optical parameters in the simulation, it is possible to match the experimental data and theoretical values. The pre-obtained calibration information was applied for post-correction to ensure accurate spectrum acquisition.

In this study, the relative reflectance was used to represent the sample signal, which was obtained by normalizing the sample spectrum to the spectrum of a bare silicon wafer; this process is similar to flat-field correction in digital imaging.[42] Note that the normalization of the sample data to the reflectance of a bare silicon wafer allows for the correction of signal distortion due to non-uniform illumination distribution or variation in the pixel-to-pixel sensitivity of the camera, thus this is an essential image analysis process to obtain an accurate spectrum. Figure 4(a) shows a flowchart of the data processing procedure for thin-film thickness measurements. In this experiment, a wafer consisting of a 400-nm-thick silicon oxide thin film on a silicon substrate is used as a sample. Figure 4(b) shows two spectrally separated beams that were simultaneously and independently captured by the two cameras suitable for the wavelength ranges of 350 to 500 nm and 500 to 1100 nm, respectively, then one can generate the single reflectance spectrum by combining each other after applying data corrections to the measured raw images. Combining data from two different SDMs is critically important, and here we explain more technical details. First, the noise reduction was performed independently by subtracting the dark noise of the system from the sample wafer as well as bare silicon wafer signals. Note that, to minimize throughput degradation, the bare silicon wafers and dark frames were measured once a day or once a week. Then, image correction was performed to obtain an accurate spectrum. The SDM is an optical system in which the image of the slit is spectrally resolved and projected onto the camera plane; the distortion, image rotation, or magnification of each module may differ

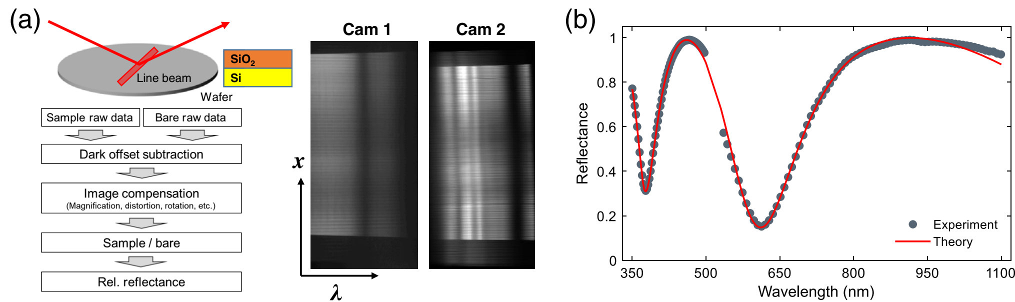


**Fig. 4** LHSI data processing and thin-film measurement. (a) Data processing flowchart for thin-film thickness measurements. The flowchart shows the data processing steps, which include corrections and noise subtraction, from the input of raw data to the output of the final spectrum. The wafer spectrum can be obtained by dividing each corrected sample signal into a bare wafer signal. Cams 1 and 2 are raw images that were measured in the range of 350 to 500 nm and 500 to 1100 nm, respectively. (b) Relative reflectance spectra for 400-nm-thick $SiO_2$ on a Si substrate wafer. The experimental data and theoretical spectra are shown as gray dots and a red line, respectively. The theoretical values were obtained by performing Fresnel coefficient calculations under the optical LHSI system conditions.

owing to differences in setup accuracy of the optical components manufacturing process. These differences cause pattern misalignment in the spectral image captured by the two cameras, and therefore it becomes difficult to measure the reliable spectrum precisely. To overcome such an issue, the final data were calibrated by dividing the compensated sample image by the compensated bare image. The relative reflectance as a function of the wavelength was extracted based on the corrected thin-film spectral image data $(x, \lambda)$ is shown in Fig. 4(b). Here, the dots and line represent the measured data and theoretical values, respectively, and we are seeing a great agreement between them. The spectral discontinuity near 500 nm was not plotted in this figure because the high-order diffracted noise observed in the 1100 nm band significantly reduced the measurement accuracy. This can be solved by applying an optimized optical design that allows the higher-order diffracted light to be filtered before it is captured by the camera. Although the spectrum was extracted from only one point in this experiment, it is possible to measure the thickness variation by performing a wide-field scan. Nevertheless, the measured thickness values were in good agreement with the theoretical values, and the basic metrology performance of the LHSI system was verified.

## 3.2 *Measurement of CD Uniformity*

In the case of existing complex semiconductor manufacturing processes, the measurement of the CD uniformity in a device cell is essential for yield enhancement. This is because the test element group no longer represents the cell pattern, and the performance of a chip depends on the CD variation.[43,44] For example, non-uniform CD distribution in the not-and flash memory (NAND) device broadens the threshold voltage distribution, increasing the typical page programming time, causing read error, and degrading device performance. Therefore, measurement of ICU in VNAND and DRAM is important, and a high spatial resolution is required to measure the spectral variation at each point in the small memory cell. In the case of OCD spectroscopy, the precision of CD variation measurement in a cell is limited because the large spot size varies from 30 to 50 $\mu$m depending on the spectral range of measurements. In contrast, the LHSI system has sufficient lateral resolution to observe spectrum variation at multiple points in a cell. Thus, the key application of the LHSI system is the measurement of both ICU and/or IWU in memory devices. In this study, we employed the LHSI system to measure the CD uniformity of the Ch.H. layers in a VNAND device. Ch.H. is a complex structure constructed by etching holes through nitride/oxide stacks to obtain conducting gate channel.[45,46] Since each layer acts as charge storage and more layers are needed to increase the memory capacitance, Ch.H. has a high aspect ratio (HAR) structure. The Ch.H. of the sixth-generation VNAND device (V6), a sample in this study, has an aspect ratio of more than 50:1, which can be estimated from the dimensions of V6,

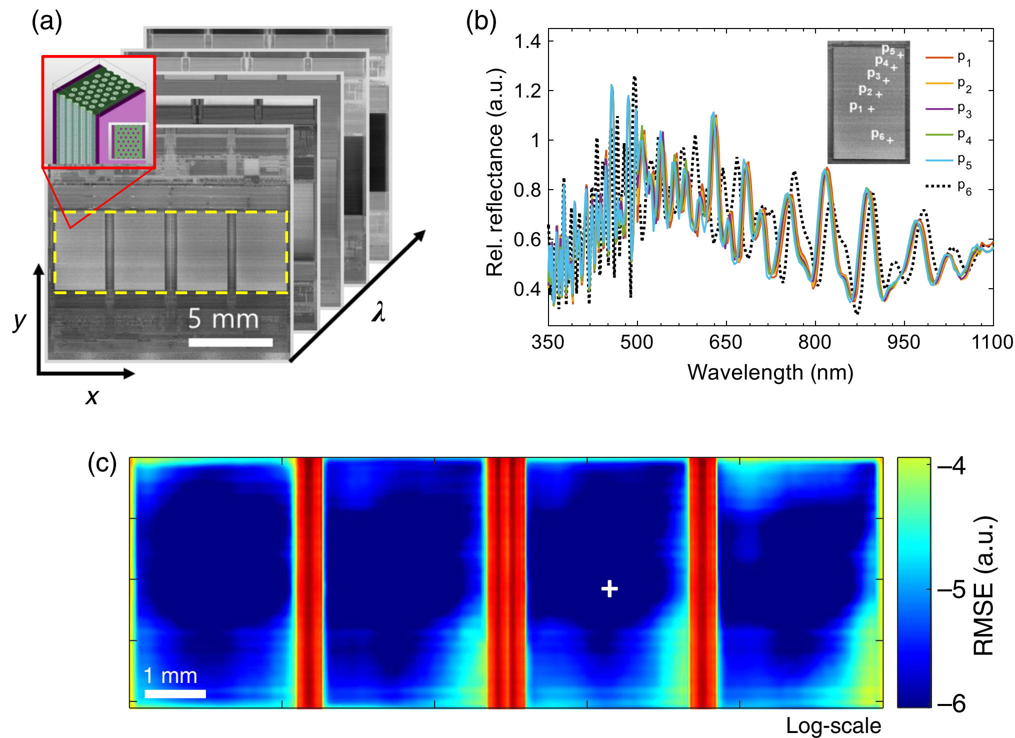


**Fig. 5** Experimental VNAND Ch.H. measurement results. (a) 3D data cube $(x, y; \lambda)$ of the LHSI system. The image size is 13 mm × 12.3 mm, and the scan time is 21 s. The 3D VNAND volume model is depicted in the red box. (b) Spectra corresponding to six different positions within a single mat; the inset shows the white crosshairs for each position. The small differences in the spectra represent the deviations in the Ch.H. overlay or CD variation. (c) RMSE heat map for the spectral skew. The reference is the spectrum extracted from the center region of the third mat. (The crosshair is shown in white.) The inter- and intra-mat color variations are related to CD uniformity. This RMSE heat map is displayed in log-scale to represent small CD changes prominently.

and has 128 to 136 layers, hole diameter of 65 to 100 nm, pillar pitch ∼150 nm, stack vertical pitch 40 to 50 nm, and total thickness 5.2 $\mu$m.[47,48] The small amount of process variation will result in CD variation, such as hole size differences or the overlay misalignment of deep Ch.H., those variations will affect the spectrum shape.

Figure 5 shows the experimental results, which demonstrate the ability of the LHSI system to measure the CD variation of four mats in one VNAND chip. Note that the chip employed in this experiment includes four mats, as described in Fig 5(a). A stack of the measured LHSI images for different wavelengths is shown in Fig. 5(a) and the FOV of the image is approximately 13 and 12.3 mm in the $x$ and $y$ directions, respectively. It is very important to mention that the line scan-based image collection was performed in the horizontal direction by applying a 13-mm line beam width to obtain the 3D imaging data with respect to $x$, $y$, and $\lambda$. The 3D imaging data required to evaluate the performance of the light source and both image sensors were acquired over a period of 21 s at a scan speed of 0.6 $\mu$m/s. In addition, the spatial resolution of 5 $\mu$m affords observation of the detailed features in a wafer and enables the measurement of the spectral distribution within a single mat. Figure 5(b) shows the reflectance spectra for the Ch.H. structure, which were measured at different positions in a mat, where the crosshair for each position from p1 to p6 is shown in the inset figure. The differences between the spectra physically represent the actual CD variation at each point. It is noteworthy that rapid reflectance changes were observed in the shorter wavelength range. In the case of the Ch.H. sample, the HAR characteristic and numerous stacked layers in Ch.H. led to such rapid spectral changes in the reflectance at each wavelength. Generally, if the spectral resolution is not sufficient to resolve the rapid oscillation in the spectrum, the measurement accuracy and sensitivity for CD variation in the device will be undesirably low due to the under-sampling. The LHSI system has a spectral

**Table 1** Comparison of the performance parameters of the conventional OCD and LHSI systems.

| Specifications | Conventional OCD | LHSI |
|---|---|---|
| Wavelength | 190 to 860 nm (SR) | 350 to 1100 nm |
| FOV | $25 \times 30\ \mu m^2$ | $13 \times 0.6\ mm^2/s$ |
| Spatial resolution | Same as FOV | 5.0 $\mu$m |
| Spectral resolution | ∼1 nm | 0.25 nm (350 to 500 nm), 0.8 nm (500 to 1100 nm) |
| Measurement | Point detection (Whiskbroom) | Line scan hyperspectral imaging (Pushbroom) |

resolution of 0.25 nm/pixel in the sub-500-nm wavelength range and it is sufficient to resolve these high-frequency changes in the reflectance. Also, the LHSI system provides a sufficient spectral resolution of 0.8 nm/pixel within the range of 500 to 1100 nm. This allows the system to achieve accurate CD uniformity for a single mat. By comparing the spectral differences at all points in the four mats shown in Fig. 5(a), the inter- and intra-mat CD uniformity could be observed. To visualize this spectral variation, the root-mean-square error (RMSE) values between the spectra were calculated, and the results are presented as a 2D heat map in Fig. 5(c). The spectrum was extracted by using all of the pixel information for each mat, and then calculating the RMSE between the spectrum for the center point in the third mat (marked with white crosshair) and each of the spectrum for the other points. Because the RMSE value between spectra is actually very small, the heat map is drawn on a logarithmic scale to emphasize the distribution. As shown in Fig 5(c), the central area of each mat has good spectral uniformity, and a large change occurs in the edge and corner region, which indicates that the Ch.H. structure in that area is different from that of the central area. In general, since cell block edges are heavily affected by optical diffraction and process effects, it is not easy to uniformly control CDs in all regions of a cell even if optical proximity correction is applied.[44] Therefore, complex CDs related to the VNAND such as hole diameter or vertical pitch can be slightly different between central and edge regions during a multiple deep Ch.H. etching processes, leading to spectrum changes representing center-to-edge CD variation. Even though the skew map does not provide detailed information on Ch.H.-related parameter variation, it acts as a simple tool to (1) verify CD uniformity in a single mat and (2) visualize mat-to-mat CD variation.

Thus far, we have introduced our LHSI metrology and demonstrated its potential as a form of next-generation measurement, which allows large areas to be scanned at high speeds, and with relatively high spatial and spectral resolution. Table 1 provides a comparison of the hardware specifications of conventional OCD spectroscopy systems and the LHSI system.[49,50]

## 4 Discussions

In this section, we discuss several technical challenges that need to be addressed to further improve the performance of LHSI technology. The LHSI system proposed in this paper is a line-beam scanning-based HSI system equipped with two SDMs for high spectral resolution. To realize higher equipment throughput than that achievable with OCD technology, the wafer scans must be performed at a higher speed. This means that the source power and frame rate of the camera must be higher. However, the throughput of the LHSI system is still insufficient owing to optical power loss in the system. The process of cropping light using apertures and a slit result in considerable optical power loss and slows down the measurement. To solve the problem of reduced throughput, even if the optical design is optimized, it is necessary to increase the source power applied to the system, which is difficult to solve in practice. As an example, LDLSs (one of the well-known broadband light sources) increase the light output power by enlarging the plasma spot.[51] However, when an optical fiber is used to apply light to the optical system, the amount of light that can be received is limited by the etendue ($\approx NA^2 \times \text{diameter}^2$ of the fiber) difference between the light source and the optical fiber, which causes optical power loss. Thus, it is essential to optimize the design of a focusing module that increases the efficiency

of fiber coupling and to develop a high-power light source by taking into consideration the etendue of the system. This would enable faster wafer measurements with a lower exposure time, where a high-speed camera is also required to increase the throughput of the entire system. The cameras implemented in the proposed LHSI system each have a large number of pixels that allow for a high spectral resolution i.e., less than 1 nm/pixel. Thus, it is necessary to develop a high-speed camera with a high pixel resolution, which is technically difficult. We estimate that, at minimum, the cameras must be capable of a resolution of more than $3200 \times 3200$ and a frame rate of at least 350 fps at full pixel resolution.

Additionally, high-quality line beams and high-performance SDMs are required to analyze the signal with high data consistency at every point in the 3D data cube. Regarding the line beam, it is necessary to ensure that the intensity across the wafer is uniformly distributed to accurately reconstruct the image and obtain precise spectral information. Fly-eye lenses are widely used to ensure the uniform spread of light intensity. However, in the case of the LHSI system, it cannot be applied to yield line beams with uniform intensity because chromatic aberration can occur, depending on the wavelength; such aberrations distort the spectrum and reconstructed image. When the square-shaped light cropped by a rectangular aperture is focused by an elliptical mirror, the intensity distribution is not symmetrical. Under such conditions, the light intensity is biased along the short axis, beginning at the center, owing to the reflection characteristics of the elliptical mirror. It is difficult to directly measure the line beam image and perform the calibration process, so it is necessary to find solutions that yield high-quality line beams under the conditions of oblique illumination configurations.

Finally, the higher-order diffracted beams must be blocked to minimize the number of spectral errors at each wavelength. When broadband light is reflected from a grating, the low-order and high-order diffracted beams are spatially mixed. Even if the intensity of the high-order diffracted light is relatively small compared to that of the low-order diffracted light, the accuracy of the spectral signal can be degraded. Thus, spectral filters should be mounted near the camera plane to ensure that only the first-order diffracted beam enters the detector.

## 5 Conclusions

We demonstrate a high-throughput LHSI reflectometry technique suitable for ICU and IWU measurements of semiconductor devices. Based on our knowledge, this is the first demonstration of developing the line-scan based HSI metrology technique for semiconductor applications, and the capability of accurately measuring the film thickness and CDs has been presented. We showed that the proposed LHSI system significantly increases the throughput of scatterometric measurements and provides both high spatial and spectral resolutions, resulting in monitoring ICU and IWU, which would be impractical with traditional scatterometry or microscopy techniques.

By employing the line-beam scanning system and advanced spectroscopic module, a massive 3D data cube $(x, y, \lambda)$ was obtained which consisted of $2440 \times 110 \times 1800$ voxels, with an FOV of $13 \times 0.6\ \mathrm{mm}^2$ and a wavelength range of 350 to 1100 nm. This 3D data cube allows for the high-throughput chip-to-chip and cell-to-cell measurement of CD uniformity in a semiconductor device. The ICU monitoring ability has been demonstrated through the measurement of thin-film wafers and patterned wafers. Furthermore, the relative reflectance, which was normalized according to the reflectance for the bare silicon wafer, was applied for spectrum analysis to reduce the optical noise and detection error. Thin-film measurement was applied as the foundation for data processing, including processes such as noise subtraction and data compensation; it was also applied to obtain accurate regression parameters to fit the experimental spectrum and model-based spectrum. This improved the measurement accuracy when the patterned wafer was measured. Additionally, the 5-$\mu$m spatial resolution was confirmed that provides detailed spatial information on patterned samples such as DRAM and VNAND memory devices, which is not feasible for conventional ellipsometric scatterometry-based systems. Regarding the FOV and spatial resolution, the sampling spot density achievable by the LHSI system was found to be more than 10,000 times higher than that of OCD-based systems, which makes ICU/IWU monitoring feasible. In this study, the VNAND wafer was measured to verify the ICU

measurement performance. Because LHSI affords high spectral and spatial resolution, the system was able to detect rapid spectral changes related to the complex structure of VNAND Ch.H. stacks. It should be noted that the spectral resolution of 0.25 nm/pixel in the wavelength range of 350 to 500 nm allowed us to observe very high-frequency spectral oscillations without generating spectral aliasing error. This high spectral resolution is one of the key advantages of the LHSI system, as it is difficult to achieve such resolving power using conventional scatterometry. Moreover, this feature is essential for accurate ICU measurement. Under the conditions of applying the IR wavelength in the LHSI system, a spectral resolution of 0.8 nm/pixel still yields relatively good spectral measurement results. However, the system design needs to be further improved to make it applicable to devices with various processing steps. Spectra were accurately extracted at arbitrary positions in the massive 3D data cubes, and with high spatial and spectral resolution. This allowed us to estimate the actual CD variation by analyzing the distribution of spectra across the scanned area. The RMSE heat map was used to visualize the spectral skew within a single mat and between different mats. This heat map also confirmed an intuitive CD variation trend, i.e., the difference in CD distribution between the center and edge of a cell block. It is believed that currently there is no technology other than LHSI that can provide the analysis for CD variation at such high levels of throughput and resolution.

In summary, given the proof-of-principle demonstration presented here for several commercial wafers, we demonstrated that the ICU and IWU can be measured at levels of precision and spectral and spatial resolution that are suitable for 3D measurements. We expect LHSI to be a reasonable tool to overcome current measurement limitations in the domain of high-volume semiconductor manufacturing.

## Acknowledgments

This work was supported by the Mechatronics Research of Samsung Electronics. The authors declare that there was no conflict of interest regarding the publication of this paper.

## References

1. "International Roadmap for Devices and Systems (IRDSTM)," *Metrology*, 2020 Edition, IEEE, Piscataway, New Jersey (2020).
2. W. H. Arnold, "Toward 3 nm overlay and critical dimension uniformity: an integrated error budget for double patterning lithography," *Proc. SPIE* **6924**, 692404 (2008).
3. M. Malloy et al., "Technology review and assessment of nanoimprint lithography for semiconductor and patterned media manufacturing," *J. Micro/Nanolithogr. MEMS MOEMS* **10**(3), 032001 (2011).
4. P. D. Bisschop et al., "Stochastic effects in EUV lithography: random, local CD variability, and printing failures," *J. Micro/Nanolithogr. MEMS MOEMS* **16**(4), 041013 (2017).
5. B. D. Bunday et al., "Determination of optimal parameter for CD-SEM measurement of line-edge roughness," *Proc. SPIE* **5375**, 515–533 (2004).
6. A. Vladár et al., "10 nm three-dimensional CD-SEM metrology," *Proc. SPIE* **9050**, 90500A (2014).
7. R. Dixson et al., "Reference metrology using a next-generation CD-AFM," *Proc. SPIE* **5375**, 633–646 (2004).
8. G. Dai et al., "Development of a 3D-AFM for true 3D measurements of nanostructures," *Meas. Sci. Technol.* **22**(9), 094009 (2011).
9. B. K. Minhas et al., "Ellipsometric scatterometry for the metrology of sub-0.1-$\mu$m-linewidth structures," *Appl. Opt.* **37**(22), 5112–5115 (1998).
10. E. Garcia-Caurel et al., "Application of spectroscopic ellipsometry and Mueller ellipsometry to optical characterization," *Appl. Spectrosc.* **67**(1), 1–21 (2013).
11. H. Huang et al., "Spectroscopic ellipsometry and reflectometry from gratings (scatterometry) for critical dimension measurement and in situ, real-time process monitoring," *Thin Solid Films* **455–456**(1), 828–836 (2004).
12. S. Ye et al., "Angle-resolved annular data acquisition method for microellipsometry," *Opt. Express*, **15**(26), 18056–18065 (2007).

13. D. Tennant, "Limits of conventional lithography," Chapter 4 in *Nanotechnology*, G. L. Timp, Ed., pp. 161–205, Springer, New York (1999).
14. B. Bunday et al., "7/5 nm logic manufacturing capabilities and requirements of metrology," *Proc. SPIE* **10585**, 1058501 (2018).
15. T-F Yao et al., "In-line metrology of nanoscale features in semiconductor manufacturing systems," *Precis. Eng.* **47**, 147–157 (2017).
16. N. Orji et al., "Metrology for the next generation of semiconductor devices," *Nat. Electron.* **1**, 532–547 (2018).
17. T. Piwonka-Corle et al., "Focused beam spectroscopic ellipsometry method and system," U.S. Patent 5608526A (1997).
18. M. Lee et al., "Imaging ellipsometry (IE)-based inspection method and method of fabricating semiconductor device by using IE-based inspection method," U.S. Patent 16/833,903 (2019)
19. D. Han et al., "Optical measuring system based on hyperspectral imaging and method of correcting the system," Korea Patent P20210003257 (2021)
20. G. Fari et al., "Hyperspectral imaging methods and apparatuses," U.S. Patent 10,838,190 (2020).
21. F. Bourcier et al., "Broadband hyperspectral spectrophotometer," U.S. Patent 16,028,695 (2020).
22. Y. Hidaka, "Spectrometer optical system, semiconductor inspection apparatus including the same and method of manufacturing semiconductor device using the apparatus," U.S. Patent 10,724,899 (2020).
23. S. Jang et al., "Inspecting apparatus based on hyperspectral imaging," U.S. Patent 16,444,719 (2021).
24. J. Son et al., "Super-resolution reflection-mode holographic microscope for 3d imaging of semiconductor devices without optical lens," *Proc. SPIE* **11245**, 1124506 (2020).
25. S. Kwon et al., "Microsphere-assisted ultra-small spot spectral reflectometry technique for semiconductor device metrology," *Proc. SPIE* **11611**, 116110G (2021).
26. Q. Li et al., "Review of spectral imaging technology in biomedical engineering: achievements and challenges," *J. Biomed Opt.* **18**(10), 100901 (2013).
27. F. Yesilkoy et al., "Ultrasensitive hyperspectral imaging and biodetection enabled by dielectric metasurfaces," *Nat. Photonics* **13**, 390–396 (2019).
28. X. Hadoux et al., "Non-invasive in vivo hyperspectral imaging of the retina for potential biomarker use in Alzheimer's disease," *Nat. Commun.* **10**, 4227 (2019).
29. Q. Li et al., "Detection of physical defects in solar cells by hyperspectral imaging technology," *Opt. Laser Technol.* **42**(6), 1010–1013 (2010).
30. X. Dong et al., "Characterization and layer thickness mapping of two-dimensional MoS2 flakes via hyperspectral line-scanning microscopy," *Appl. Phys. Express* **12**(10), 102004 (2019).
31. B. Gawlik et al., "Hyperspectral imaging for high-throughput, spatially resolved spectroscopic scatterometry of silicon nanopillar arrays," *Opt. Express* **28**(10), 14209–14221 (2020).
32. D. Kim et al., "LASIE: large area spectroscopic imaging ellipsometry for characterizing multi-layered film structures," *Int. J. Precis. Eng. Manuf.* **19**(8), 1125–1132 (2018).
33. X. Dong et al., "Line-scan hyperspectral imaging microscopy with linear unmixing for automated two-dimensional crystals identification," *ACS Photonics* **7**(5), 1216–1225 (2020).
34. D. Cho et al., "High-speed wafer film measurement with heterogeneous optical sensor system," *Proc. SPIE* **11611**, 116110H (2021).
35. X. Dong et al., "Hyperspectral fingerprints for atomic layer mapping of two-dimensional materials with single-layer accuracy," *J. Phys. Chem. C* **125**, 16583–16590 (2021).
36. J. Jung et al., "A breakthrough on throughput and accuracy limitation in ellipsometry using self-interference holographic analysis," *Proc. SPIE* **11611**, 116111J (2021).
37. W. Kim et al., "A new approach in optical metrology with multi-angle information through self-interferometric ellipsometry," *Proc. SPIE* **11817**, 1181707 (2021).
38. J. Kim et al., "Hyperspectral imaging reflectometry for 3D semiconductor metrology," in *Conf. Lasers and Electro-Opt.*, p. AM1R.2 (2021).

39. D. J. Griffiths, *Introduction to Electrodynamics*, 4th ed., Cambridge University Press, Cambridege, England (2017).
40. S. Kim et al., "Design and construction of an Offner spectrometer based on geometrical analysis of ring field," *Rev. Sci. Instrum.* **85**(8), 083108 (2014).
41. D. Semwogerere et al., "Confocal microscopy," in *Encyclopedia of Biomaterials and Biomedical Engineering*, 2nd ed., G. E. Wnek and G. L. Bowlin, Eds., CRC Press, Boca Raton, Florida (2008).
42. J. A. Seibert et al., "Flat-field correction technique for digital detectors," *Proc. SPIE* **3336**, 348–354 (1998).
43. S. Kwon et al., "Microsphere-assisted, nanospot, non-destructive metrology for semiconductor devices," *Light Sci. Appl.* **11**, 32 (2022).
44. Y. Kim et al., "The cell pattern correction through design-based metrology," *Proc. SPIE*, **9427**, 942713 (2015).
45. A. Goda, "Recent progress on 3D NAND flash technologies," *Electronics* **10**(24), 3156 (2021).
46. G. H. Lee et al., "Architecture and process integration overview of 3D NAND flash technologies," *Appl. Sci.* **11**(15), 6703 (2021).
47. Y.D. Chen, "Advanced patterning techniques for 3D NAND devices," Coventor, 2019, http://www. coventor.com/blog/advanced-patterning-techniques-3d-nand-devices/.
48. M. Lapedus, "3D NAND flash wars begin," SemiEngineering, 2018, http://semiengineering .com/3d-nand-flash-wars-begin/.
49. J. A. Woollam Co., *RC2 Ellipsometer Brochure*, Lincoln, Nebraska (2017).
50. A. D. Boef et al., "Scatterometry for advanced process control in semiconductor device manufacturing," *Proc. SPIE* **10449**, 1044916 (2017).
51. Energetiq Technology, Inc., LDLS Catalog, Wilmington, Massachusetts, http:/www .energetiq.com/ (2021).

**Changhyeong Yoon** works as a staff engineer at Mechatronics Research in Samsung Electronics. He received his BS and MS degrees in physics from Korea University in 2010 and 2012, respectively, and his PhD in bioimaging from Korea University in 2018. He has reported several papers about imaging through a scattering medium, imaging reconstruction using a transmission matrix approach, and optical aberration correction. His current research interests include optical scatterometry, ellipsometry, and computational imaging.

**Daehoon Han** also works as a staff engineer at Mechatronics Research in Samsung Electronics. He received his BS degree in physics from Dongguk University in 2008 and his integrated PhD in Terahertz spectroscopy from KAIST in 2016. He is currently developing the state of the art snapshot polarimeter.

**Myungjun Lee** is a head of group at Samsung Electronics. He received his BE, MS, and PhD degrees in electrical computer engineering/optical science from University of Arizona, Texas A&M, Korea University, in 2002, 2005, 2010, respectively. Previously, he worked for KLA-Tencor, GlobalFoundries, and Nanometric, and was a postdoctoral fellow at UCLA. He has authored/co-authored 50+ papers, and holds 30+ US patents in various optical system designs and their applications for imaging, sensing, communications, semiconductor patterning, and metrology.

Biographies of the other authors are not available.